The Cryosphere, 20, 5475–5490, 2026
https://doi.org/10.5194/tc-20-5475-2026

The Cryosphere
Open Access

Impact of climate forcing time step in an ice-sheet firn model

Tesse E. A. van den Aker[1], **Peter Kuipers Munneke**[1], **Willem Jan van de Berg**[1], **Walter W. Immerzeel**[2], **and Michiel R. van den Broeke**[1]

[1]Institute for Marine and Atmospheric Research, Utrecht University, Utrecht, the Netherlands
[2]Department of Physical Geography, Utrecht University, Utrecht, the Netherlands

Correspondence: Tesse E. A. van den Aker (t.e.a.vandenaker@uu.nl)

Received: 26 January 2026 – Discussion started: 19 February 2026
Revised: 13 August 2026 – Accepted: 28 August 2026 – Published: 24 September 2026

Abstract. The firn layer regulates how an ice sheet responds to atmospheric climate change by modifying how changes in surface temperature, snow accumulation and ablation affect the ice-sheet mass balance. Firn properties are often simulated with a firn densification model. Prior studies have used a variety of time steps in the climate forcings of such firn models, ranging from 3 h to 1 d, 1-month, or even annual. The climate forcing time step impacts the creation of pore space by snow accumulation and the depletion of pore space by snowmelt and firn densification. To investigate this effect, we force the firn densification model IMAU-FDM with surface mass balance components and meteorological variables at different time steps for the Antarctic Peninsula and southern Greenland Ice Sheet. We show that the final modelled firn layer contains more pore space for larger forcing time steps, and that the magnitude of this effect depends on the climate regime. Locations with limited firn pore space due to seasonal melt, and regions with emerging firn aquifers, are most sensitive. The key in causing the differences in firn pore space is the presence or absence of a diurnal cycle in the input data. A climate forcing time step equal to or greater than a day allows for a non-physical coexistence of snowmelt and sub-zero surface temperatures, leading to immediate shallow refreezing of meltwater. Subsequent melting removes refrozen higher density firn rather than porous firn, reducing the amount of firn air that is lost through melting. Therefore, for locations experiencing surface melt, the decoupled temperature and snowmelt in the upper layers results in more firn air with a climate forcing time step equal to or greater than a day. We also found that model parameterizations can become unsuitable when applied outside the physical conditions or climate forcing time step on which they are based, leading to unrealistic firn densification behavior in the model. We argue that (1) firn models forced with surface mass balance terms and meteorological variables require a timestep small enough to capture at least the diurnal cycle, (2) parameterizations should be used in a way that is consistent with the development data.

1 Introduction

Firn, the transitional state between snow and glacial ice, covers ∼ 90 % of the Greenland Ice Sheet (GrIS) (Noël et al., 2022) and ∼ 99 % of the Antarctic Ice Sheet (AIS) (Winther et al., 2001). Firn contains air that prevents a fraction of the meltwater to run off into the ocean, either by refreezing or liquid water retention. Approximately ∼ 39 % of surface meltwater on the GrIS and ∼ 94 % on the AIS is retained in the firn (Medley et al., 2022). Consequently, the firn layer keeps meltwater away from crevasses, where it could otherwise enter the GrIS subglacial drainage system, or engage in hydrofracturing on Antarctic ice shelves. Also, outside the percolation zone the firn layer evolution is of relevance, as variations in firn mass and thickness complicate the interpretation of altimetry observations for ice-sheet mass balance.

Firn models are used to improve our understanding of physical processes, to interpret observations including remote sensing data, and to make projections of ice-sheet surface mass balance (SMB) in the future (The Firn Symposium Team, 2024). Firn models differ in their parameterizations and formulations for densification, thermodynamics, and water percolation processes (Vandecrux et al., 2020). Although a variety of firn models exist, all models have in common that they use numerical methods to integrate a set of coupled

Published by Copernicus Publications on behalf of the European Geosciences Union.

differential equations in time. In this paper, we focus on the fact that the upper boundary conditions for solving the equations are provided at a discrete time step. Those boundary conditions can be components of the SMB and/or surface energy balance (SEB), or meteorological variables, which varies depending on the firn model (The Firn Symposium Team, 2024). The climate forcing time step differs greatly across studies, varying from 1 h, to days, months, and even years (Sørensen et al., 2011; Simonsen et al., 2013; Langen et al., 2017; Meyer and Hewitt, 2017; Verjans et al., 2019; Stevens et al., 2020; Brils et al., 2022; Gkinis et al., 2021; Medley et al., 2022; Thompson-Munson et al., 2023; Veldhuijsen et al., 2023; Wever et al., 2023; Hansen et al., 2024; Zhang et al., 2024). Here, we focus on the climate forcing time step for the IMAU firn densification model (IMAU-FDM), which is forced with SMB and meteorological variables at the upper boundary.

Reasons for choosing a certain climate forcing time step are most often practical: the data are not available at smaller time steps, the amount of forcing data becomes too large, or the computational resources are insufficient. Evaluation of the forcing time step is often absent or based on differing lines of reasoning. For example, Medley et al. (2022) argue that the absence of a diurnal cycle in the forcing time step is a limitation of their model, whereas Meyer and Hewitt (2017) expect that the daily cycle influences only the uppermost meter of the firn column, and therefore, ignore it.

We emphasize the difference between the time step used to solve the differential equations in a model, and the time step at which the forcing data is provided. The focus of this paper is on the latter. Most often, the model time step is smaller than the forcing data time step. To clarify with an example, Veldhuijsen et al. (2023) uses a 3-hourly climate forcing linearly interpolated to a 15 min model time step.

In this paper, we demonstrate that the output of a firn model is sensitive to the forcing time step when forced with SMB and meteorological variables at the surface, while geographically focusing on the Antarctic Peninsula Ice Sheet (APIS) and the southern GrIS.

2 Methods: Firn modelling setup

We use IMAU-FDM (Brils et al., 2022; Veldhuijsen et al., 2023) to simulate the firn layer and investigate the sensitivity of the modelled firn layer to the climate forcing time step. This section describes IMAU-FDM and specifies similarities and differences in the model for the two domains. We also describe the forcing dataset, setup for testing different forcing time steps, model initialization, and study areas.

2.1 IMAU-FDM

IMAU-FDM is a 1D semi-empirical model that simulates density, temperature, and meltwater content in the firn layer. The model is originally developed by Helsen et al. (2008) and has undergone multiple updates (Ligtenberg et al., 2014; Brils et al., 2022; Veldhuijsen et al., 2023). We use IMAU-FDM v1.2A (Veldhuijsen et al., 2023) for the Antarctic domain and IMAU-FDM v1.2G (Brils et al., 2022) for the Greenland domain, which only differ from each other in their ice-sheet dependent calibration. Both versions have been evaluated extensively against firn density and temperature observations (Ligtenberg et al., 2014; Kuipers Munneke et al., 2015; Brils et al., 2022; Veldhuijsen et al., 2023).

The firn and ice column are divided into 200–3000 layers, traced in a Lagrangian framework. Snowfall is added to the topmost layer of the column, burying other layers and thereby representing downward advection. No layers are removed during a simulation. The layers have a maximum vertical resolution of 0.15 m. Layer routines are built in that split the uppermost layer if it exceeds the 0.15 m threshold and merges the two uppermost layers if the thickness of the uppermost layer is smaller than 0.05 m. When the firn column has less than 200 layers, 100 very thin layers of pure ice are added to the bottom of the column.

The fresh snow density is an upper boundary condition with different parameterizations for the AIS and GrIS domain. In IMAU-FDM v1.2A (AIS), the fresh snow density ρ_0 ($\mathrm{kg\,m^{-3}}$) depends on instantaneous surface temperature T_s (K) and 10 m wind speed $f\!f_{10\,\mathrm{m}}$ ($\mathrm{m\,s^{-1}}$) (Eq. 1) (Lenaerts et al., 2012; Veldhuijsen et al., 2023):

$$\rho_0 = 82.97 + 0.769 T_\mathrm{s} + 11.67 f\!f_{10\,\mathrm{m}} \tag{1}$$

In IMAU-FDM v1.2G (GrIS), ρ_0 is based on the surface temperature averaged over the year prior to the snowfall $\overline{T_\mathrm{s}}$ (K) (Eq. 2) (Fausto et al., 2018; Brils et al., 2022):

$$\rho_0 = 362.1 + 2.78(\overline{T_\mathrm{s}} - 273.15) \tag{2}$$

The densification of snow and the underlying firn in each layer is parameterized by a semi-empirical equation (Eq. 3) based on Arthern et al. (2010):

$$\frac{\mathrm{d}\rho}{\mathrm{d}t} = D\dot{b}g\mathrm{MO}(\rho_\mathrm{i} - \rho)\mathrm{e}^{-\frac{E_\mathrm{c}}{RT} + \frac{E_\mathrm{g}}{RT_\mathrm{b}}} \tag{3}$$

with $\dot{b}$ the average accumulation rate ($\mathrm{kg\,m^{-2}\,yr^{-1}}$) over the spin-up period, g the gravitational acceleration ($9.81\,\mathrm{m\,s^{-2}}$), ρ_i the density of bubble-free ice ($917\,\mathrm{kg\,m^{-3}}$), ρ the instantaneous layer density ($\mathrm{kg\,m^{-3}}$), E_c the activation energy for creep ($60\,000\,\mathrm{J\,mol^{-1}}$), E_g the activation energy for grain growth ($42\,400\,\mathrm{J\,mol^{-1}}$), R the universal gas constant ($8.3145\,\mathrm{J\,mol^{-1}\,K^{-1}}$), T the instantaneous layer temperature (K), and T_b the instantaneous temperature of the bottom firn layer. D is a constant and MO is a correction term that improves model alignment with observations of the 550 and $830\,\mathrm{kg\,m^{-3}}$ density level depths (Ligtenberg et al., 2011). The correction term differs for both domains (Brils et al., 2022; Veldhuijsen et al., 2023). In this equation, $\mathrm{e}^{\frac{-E_\mathrm{c}}{RT}}$

represents the temperature-dependency of ice deformation; $e^{\frac{E_g}{RT_b}}$ is a correction term arising from the estimated grain size ($E_c > E_g$). Ice grains grow faster in warmer conditions, while large grains deform slower than smaller grains, hence reducing the densification. As the current grain size is the result of the grain growth since deposition, its impact on densification must be approximated by the typical temperature conditions. Therefore, the mean firn temperature, estimated by the temperature of the lowermost layer (T_b), is used in Eq. (3).

The physical description for water percolation and heat transport is identical in both model versions. Liquid water is added to the top of the column. Its transport through the layers is calculated using the "bucket scheme". In this scheme, each layer has an irreducible water content which is the maximum amount of water that can be retained by capillary forces. The irreducible water content decreases with increasing density (Coléou and Lesaffre, 1998). Water refreezes when in a firn layer cold content is available, reducing the pore space of the firn.

In IMAU-FDM, ice layers form through subsequent events of wetting and refreezing, whereby the density is increased and the pore space is reduced until the ice density of $917\,\mathrm{kg\,m^{-3}}$ is reached. Ice layers primarily form near the surface where sufficient meltwater and cold content allow for repeated cycles of pore space filling and refreezing. Therefore, in the current model setup, a single melt event cannot completely fill and refreeze the pore space of a firn layer. The bucket scheme does not allow standing water over ice layers. Instead, water percolates to the next layer when no pore space is available. The water percolation formulation implies that, in one model time step, water can percolate through the whole firn layer until it reaches the firn-ice interface. Any leftover water is assumed to run off.

Heat conduction through the firn layer is described by the 1D heat transfer equation, with conductivity being a function of density (Calonne et al., 2019; Brils et al., 2022). Refreezing acts as a heat source within the firn. Heat transfer at the upper boundary is governed by the prescribed surface temperature. A constant heat flux through the bottom layer is applied as the lower boundary condition.

2.2 Forcing dataset

IMAU-FDM is forced at the surface with surface temperature, 10 m wind speed, snowmelt, snowfall, sublimation, snowdrift erosion, and rainfall. These climate forcings originate from the regional atmospheric climate model RACMO2.3p2 (Noël et al., 2018; Van Wessem et al., 2018), dynamically downscaling ERA5 reanalysis data (Hersbach et al., 2020). The AIS data covers the period 1979–2023 with a horizontal resolution of 27 km × 27 km and is extended from Van Wessem et al. (2018). The GrIS data spans 1 September 1939–1 December 2023 with a horizontal resolution of

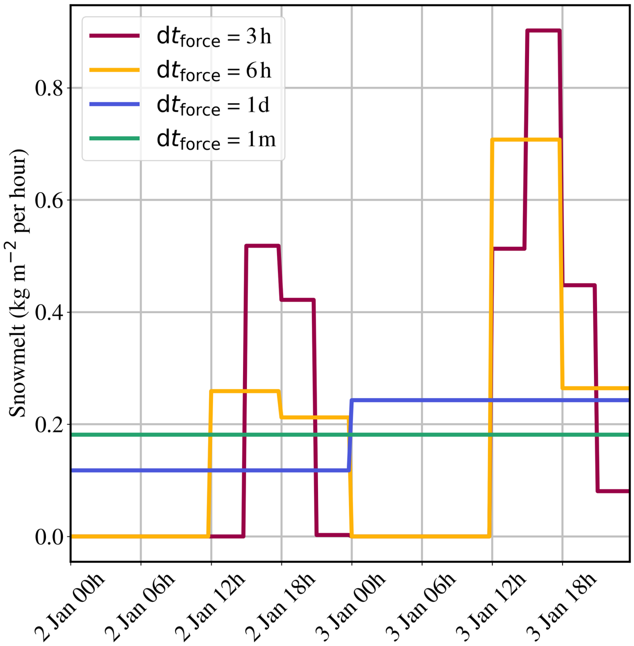

Figure 1. Example of 48 h of snowmelt forcing at $dt_{force} = 3$, 6 h, 1 d, and 1 m. The graph also visualizes the model's interpolation of the forcing onto a 15 min timestep. Note the presence of a diurnal cycle in the snowmelt input for $dt_{force} = 3$ and 6 h and its absence for $dt_{force} = 1$ d and 1 m.

5.5 km × 5.5 km and is a renewed and extended version of the simulation presented by Noël et al. (2018).

2.3 Climate forcing time step

We force the model with four climate forcing time steps (dt_{force}) at the surface: 3 h, 6 h, 1 d and 1-month, referred to as $dt_{force} = 3$ h, 6 h, 1 d, and 1 m respectively. We chose these values because (1) they are typically used to force firn models, and (2) they provide examples with and without a diurnal cycle in the input data (Fig. 1). In addition, $dt_{force} = 3$ h is the smallest available climate forcing time step from RACMO2.3p2 and is commonly used to force IMAU-FDM. We averaged the 3-hourly surface mass fluxes, surface temperature, and 10 m wind speed data to get the input data for $dt_{force} = 6$ h, 1 d, and 1 m. IMAU-FDM interpolates the forcing data onto a 15 min model time step in which we assume a constant value for the whole forcing period for the surface mass fluxes, surface temperature and 10 m wind speed (Fig. 1). To summarize, numerical time integration is done using a model time step of 15 min, but the climate forcing time step can be 3 h, 6 h, 1 d, or 1-month.

2.4 Initialization

In IMAU-FDM, the firn layer is initialized by spinning up the model over a repeated reference period until it reaches a steady state where the firn air content (FAC) and surface height no longer change. FAC is the vertically integrated pore space in a column expressed in meters, representing the change in depth that would result from compressing the firn layer to the density of glacier ice (here assumed to be $910\,\mathrm{kg\,m^{-3}}$). The full firn layer, up to the pore close-off density of $830\,\mathrm{kg\,m^{-3}}$, is refreshed during the initialization. To avoid shocks after the initialization, this reference period should not exhibit large climate trends. The AIS spin-up period covers 1979–2020 (Veldhuijsen et al., 2023). After 2020, the AIS has gained mass due to higher than average precipitation (Wang et al., 2023), and therefore 2020–2023 is excluded from the spin-up period. The GrIS SMB has been decreasing since 1990 (Shepherd et al., 2012). Therefore, we chose 1 September 1939–31 December 1970 as the reference period. The climate forcing time step was identical for spin-up and the rest of the simulation.

2.5 Study areas: APIS and southern GrIS

We select the APIS and the southern GrIS, two areas with a broad range of surface climate conditions, from low to high accumulation and with and without melt (Fig. 2). Accumulation represents the net result of snowfall, sublimation and drifting snow processes (deposition/erosion).

In the APIS, the main climate gradient is from the wet and warm west to the dry and cold east. The ice shelves are the lowest-lying areas (Fig. 2a) and experience most snowmelt (up to $500\,\mathrm{kg\,m^{-2}\,yr^{-1}}$) (Fig. 2b), whereas the snowmelt is limited on the higher-elevated grounded ice. In contrast, the grounded ice has higher accumulation, peaking in the northwest of the APIS. Accumulation is lower on the ice shelves (Fig. 2c).

In the southern GrIS, the lowest-lying marginal areas (Fig. 2d) experience most snowmelt ($> 750\,\mathrm{kg\,m^{-2}\,yr^{-1}}$) (Fig. 2e). Accumulation is highest in the east ($> 2000\,\mathrm{kg\,m^{-2}\,yr^{-1}}$) (Fig. 2f). Snowmelt rates exceeding $500\,\mathrm{kg\,m^{-2}\,yr^{-1}}$ combined with high accumulation, as in the southeastern GrIS, typically results in firn aquifers, or, in drier climate zones like the southwest, in ice slabs (Brils et al., 2024).

3 Effect of climate forcing timestep on firn

We look into the FAC for $\mathrm{d}t_{\mathrm{force}} = 3\,\mathrm{h}$ and compare this to FAC with larger $\mathrm{d}t_{\mathrm{force}}$. We show that increasing $\mathrm{d}t_{\mathrm{force}}$ leads to more firn pore space. We present maps of FAC for different $\mathrm{d}t_{\mathrm{force}}$ to understand how climate regimes and $\mathrm{d}t_{\mathrm{force}}$ influence the FAC, showing the relevance of identifying the processes responsible for these differences. We discuss how these processes depend on the $\mathrm{d}t_{\mathrm{force}}$ and how this affects the depletion or creation of pore space. In this section we focus on the effect on total FAC, an important quantity for retention studies.

In the discussion of these results, we use the following abbreviations: $\mathrm{FAC_{3\,h}}$, $\mathrm{FAC_{6\,h}}$, $\mathrm{FAC_{1\,d}}$, and $\mathrm{FAC_{1\,m}}$ correspond to the FAC at $\mathrm{d}t_{\mathrm{force}} = 3\,\mathrm{h}$, 6 h, 1 d, and 1 m respectively. The $\mathrm{FAC_{3\,h}}$ compared to FAC simulated at a larger $\mathrm{d}t_{\mathrm{force}}$, is defined as $\Delta\mathrm{FAC_{6\,h}} = \mathrm{FAC_{6\,h}} - \mathrm{FAC_{3\,h}}$, $\Delta\mathrm{FAC_{1\,d}} = \mathrm{FAC_{1\,d}} - \mathrm{FAC_{3\,h}}$, and $\Delta\mathrm{FAC_{1\,m}} = \mathrm{FAC_{1\,m}} - \mathrm{FAC_{3\,h}}$. ΔFAC (without subscript) denotes the difference between $\mathrm{FAC_{3\,h}}$ and FAC modelled with larger $\mathrm{d}t_{\mathrm{force}}$. A positive ΔFAC thus indicates more pore space for the larger climate forcing time step.

3.1 $\mathrm{FAC_{3\,h}}$ and ΔFAC

Figure 3 shows the $\mathrm{FAC_{3\,h}}$ (Fig. 3a and e), $\Delta\mathrm{FAC_{6\,h}}$ (Fig. 3b and f), $\Delta\mathrm{FAC_{1\,d}}$ (Fig. 3c and g), and $\Delta\mathrm{FAC_{1\,m}}$ (Fig. 3d and h) for the APIS and southern GrIS. Figure 3b, c, d, f, g, and h show that $\mathrm{FAC_{3\,h}}$ is generally lower than FAC with larger $\mathrm{d}t_{\mathrm{force}}$ in both the APIS and southern GrIS. The larger the $\mathrm{d}t_{\mathrm{force}}$ becomes, the higher the ΔFAC.

On the APIS, FAC is smallest (0–5 m for $\mathrm{FAC_{3\,h}}$) in the lower-lying areas, corresponding to the ice shelves (Fig. 3a). ΔFAC is largest on the ice shelves (15 % for $\Delta\mathrm{FAC_{1\,d}}$, increasing up to 44 % for $\Delta\mathrm{FAC_{1\,m}}$). $\Delta\mathrm{FAC_{6\,h}}$ is relatively small (3 %). Interestingly, an area with a negative ΔFAC is situated along the high-elevation southern spine of the APIS (red hues in Fig. 3b–d). In a relative sense, these differences are small, of the order of $\sim 0.5\,\mathrm{m}$ on typical $\mathrm{FAC_{3\,h}}$ values of 15–20 m. In both an absolute and a relative sense, ΔFAC is largest for the locations with low $\mathrm{FAC_{3\,h}}$.

In the southern GrIS, FAC increases from the ice margin where it equals zero in the ablation zone, to higher elevations, with the steepest spatial gradients on the east coast (Fig. 3e). In the southern GrIS, in the ablation zone, most clearly visible on the western margin, ΔFAC is small (Fig. 3f–h). Here, firn pore space is depleted across all simulations, regardless of $\mathrm{d}t_{\mathrm{force}}$. At high elevations ($> 2000\,\mathrm{m}$), ΔFAC is also relatively small, with average differences $< 1\,\%$ in $\Delta\mathrm{FAC_{6\,h}}$ up to 3 % in $\Delta\mathrm{FAC_{1\,m}}$. At intermediate elevations, a band with larger ΔFAC is apparent, increasing with greater $\mathrm{d}t_{\mathrm{force}}$ (Fig. 3f, g, and h). In the east and west, ΔFAC in this band is quite similar in an absolute sense: on average, $\Delta\mathrm{FAC_{6\,h}} = 0.3\,\mathrm{m}$, $\Delta\mathrm{FAC_{1\,d}} = 2.1\,\mathrm{m}$, and $\Delta\mathrm{FAC_{1\,m}} = 4.0\,\mathrm{m}$. However, relative differences are larger in the west, where absolute $\mathrm{FAC_{3\,h}}$ values are much smaller (typically $< 20\,\mathrm{m}$) than in the east (typically $> 20\,\mathrm{m}$).

3.2 Processes responsible for ΔFAC in IMAU-FDM

We discuss the processes that contribute to ΔFAC in IMAU-FDM. Figure 4 gives an overview of the dominant processes in a firn layer that cause the forcing time step dependency of the FAC and that are described in depth later in this section. The processes described below are computed every 15 min model time step during both the spin-up and the simulation periods.

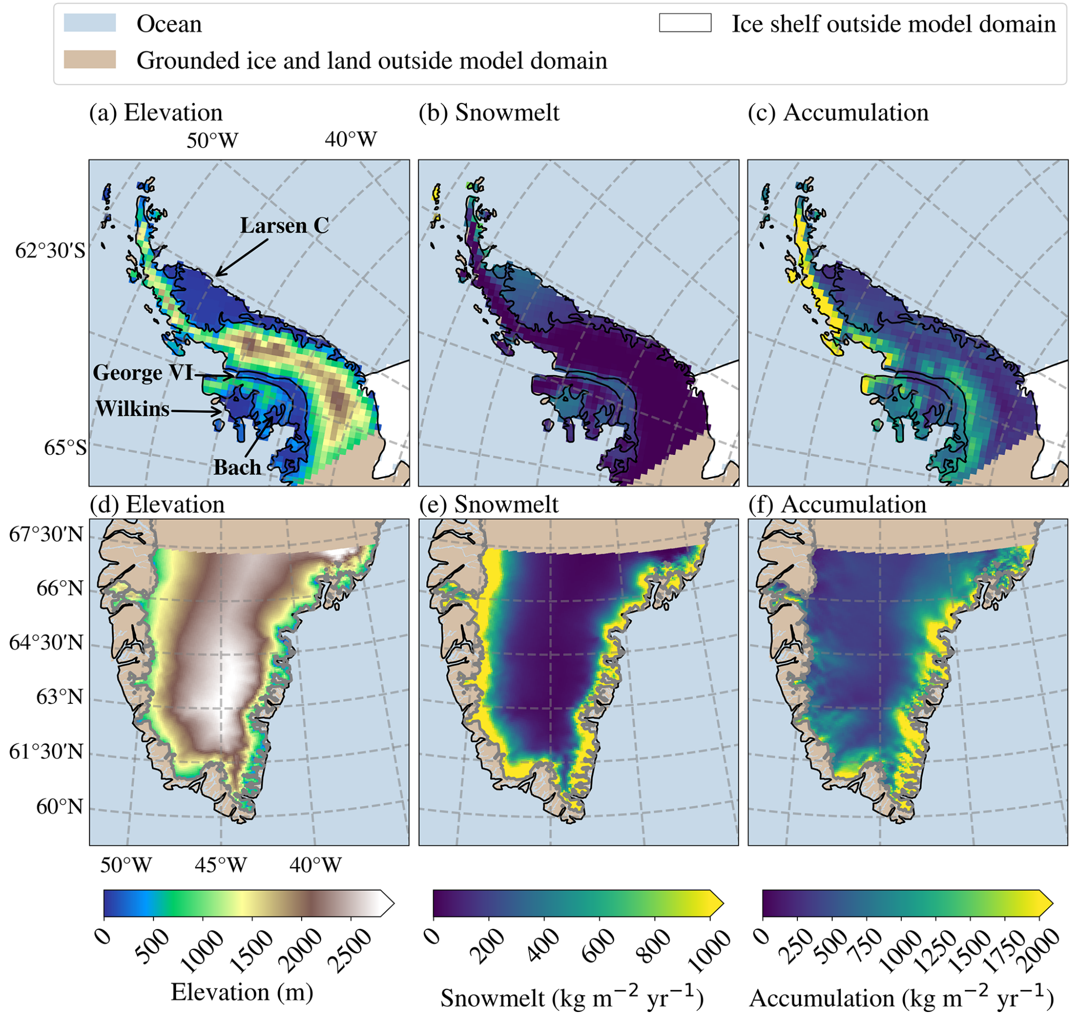

Figure 2. Maps showing elevation **(a, d)**, snowmelt averages **(b, e)**, and accumulation averages **(c, f)** for the modelled domain in the APIS **(a–c)** and southern GrIS **(d–f)** during the spin-up period, i.e. 1979–2020 for the APIS and 1 September 1939–31 December 1970 for the southern GrIS. The black contours show the coastal and ice shelf boundaries in the APIS **(a–c)** and the coastal boundaries in the southern GrIS **(d–f)**. Ice shelf names within the model domain are indicated for the APIS **(a)**. Gray contours show the ice mask boundaries in southern GrIS **(d–f)**.

FAC is governed by a balance between the processes that create pore space (snowfall) and that deplete it (densification, snowmelt, snowdrift erosion, and sublimation). Figure 5 shows the relative importance of several processes determining $\mathrm{FAC}_{3\,\mathrm{h}}$ and $\mathrm{FAC}_{1\,\mathrm{d}}$ for two example locations depicted in Fig. 3. Figure 5a represents a location in the APIS and Fig. 5b a location in the southern GrIS. Both locations experience similar melt and $\Delta\mathrm{FAC}_{1\,\mathrm{d}}$, but the location on the GrIS has more snowfall. For clarity, a positive excursion of the elevation change difference in Fig. 5c and d means that the elevation increases more for $\mathrm{d}t_{\mathrm{force}} = 1\,\mathrm{d}$.

Snowfall is the major source of firn air in both locations (Fig. 5a and b). The contribution of snowfall to FAC for the APIS is slightly higher for $\mathrm{d}t_{\mathrm{force}} = 3\,\mathrm{h}$ than for $\mathrm{d}t_{\mathrm{force}} = 1\,\mathrm{d}$ (Fig. 5c), whereas it is almost the same for the GrIS (Fig. 5d). Larger differences arise for processes that reduce FAC. In both locations, more $\mathrm{FAC}_{3\,\mathrm{h}}$ is removed by snowmelt than $\mathrm{FAC}_{1\,\mathrm{d}}$ (Fig. 5c and d). For the dry location (Fig. 5a), densification is relatively slow, and FAC depletion due to melt is largest. For the wet location (Fig. 5b), the densification dominates reduction of the FAC. At both locations, melt removes more $\mathrm{FAC}_{3\,\mathrm{h}}$ and has slower firn densification at $\mathrm{d}t_{\mathrm{force}} = 3\,\mathrm{h}$ (Fig. 5c and d).

Summarizing, ΔFAC is mainly controlled by melt and densification rate, with a minor contribution from snowfall. Now, we further zoom in on those processes to understand the ΔFAC they cause.

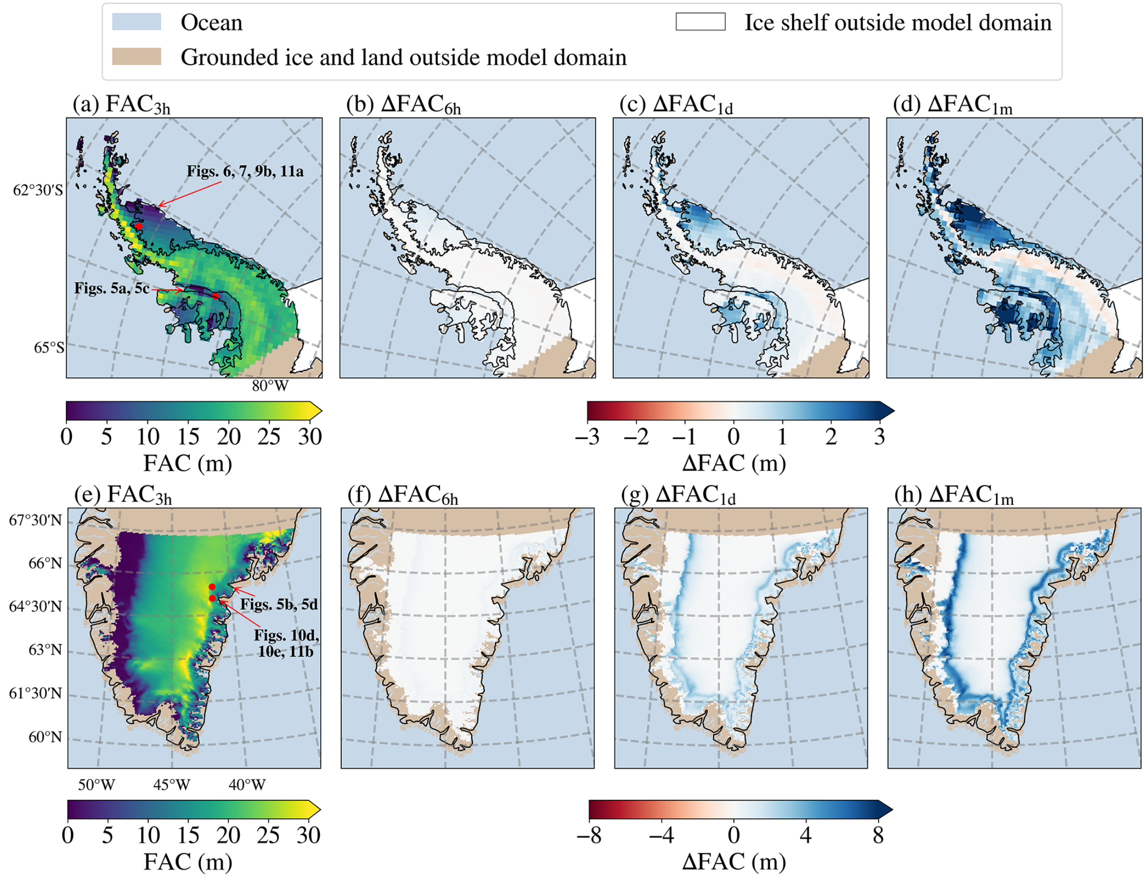

Figure 3. Maps showing average $FAC_{3\,h}$ **(a, e)**, along with average $\Delta FAC_{6\,h}$ **(b, f)**, $\Delta FAC_{1\,d}$ **(c, g)**, and $\Delta FAC_{1\,m}$ **(d, h)** in the APIS **(a–d)** and southern GrIS **(e–h)**. The averages are over the whole simulation period, i.e. 1979–2023 for the APIS and 1 September 1939–31 December 2023 for the southern GrIS. The red dots highlighted in panel **(a)** and **(e)** are used as example locations later in this paper.

3.2.1 Process 1: melt

Melt provides the largest contribution to ΔFAC, simulations with $dt_{force} = 3\,h$ have more FAC reduction than for larger dt_{force} (Fig. 5c and d). Climate zones with more melt, have a higher ΔFAC. We identify two types of melt-related mechanisms responsible for ΔFAC, namely a surface-based process and a process occurring at depth.

At the surface, the model is forced with a melt flux, and firn in the top layer is converted to liquid water. The subsequent fate of the meltwater depends on dt_{force}. With a diurnal cycle in dt_{force}, i.e. 3- and 6 h, surface temperatures reach 0 °C during melt events. Therefore, the water cannot immediately refreeze and the timing of refreezing and snowmelt in the top layer alternate between day and night (Fig. 6a). In contrast, without a diurnal cycle in dt_{force}, i.e. 1 d and 1-month, surface melt and temperature become decoupled. As a result, melt can occur at subfreezing surface temperatures and the meltwater that can be retained in the pore space refreezes immediately near the surface (Fig. 6b). This leads to a higher near-surface density under larger dt_{force} (Fig. 6c). Subsequent melt events convert firn to liquid water again and remove less pore space when a high-density surface layer is present, as in $dt_{force} = 1\,d$ and 1 m. This melt and surface temperature interaction in absence of a daily cycle is the main mechanism that leads to higher ΔFAC with increasing dt_{force} (Fig. 4, process 1).

The second process is that meltwater percolates deeper at $dt_{force} = 3\,h$; less water that can be retained in the pore space is immediately refrozen near the surface. Consequently, refreezing occurs deeper if there is enough cold content (Figs. 7a and b and 4 process 1). The latent heat released by refreezing at depth is trapped due to the low thermal conductivity of firn. Thus, the deeper firn for $dt_{force} = 3\,h$ is warmer (Fig. 7c and d). Warmer firn enhances firn densification, as discussed in the following subsection.

3.2.2 Process 2: firn densification

Several processes contribute to the firn densification rate. First, more snowfall leads to more firn that can densify (contribution of snowfall to $\dot{b}$ in Eq. 3). Simulations with larger dt_{force} have more FAC (Fig. 3), and therefore undergo more densification (Figs. 5 and 4, process 2).

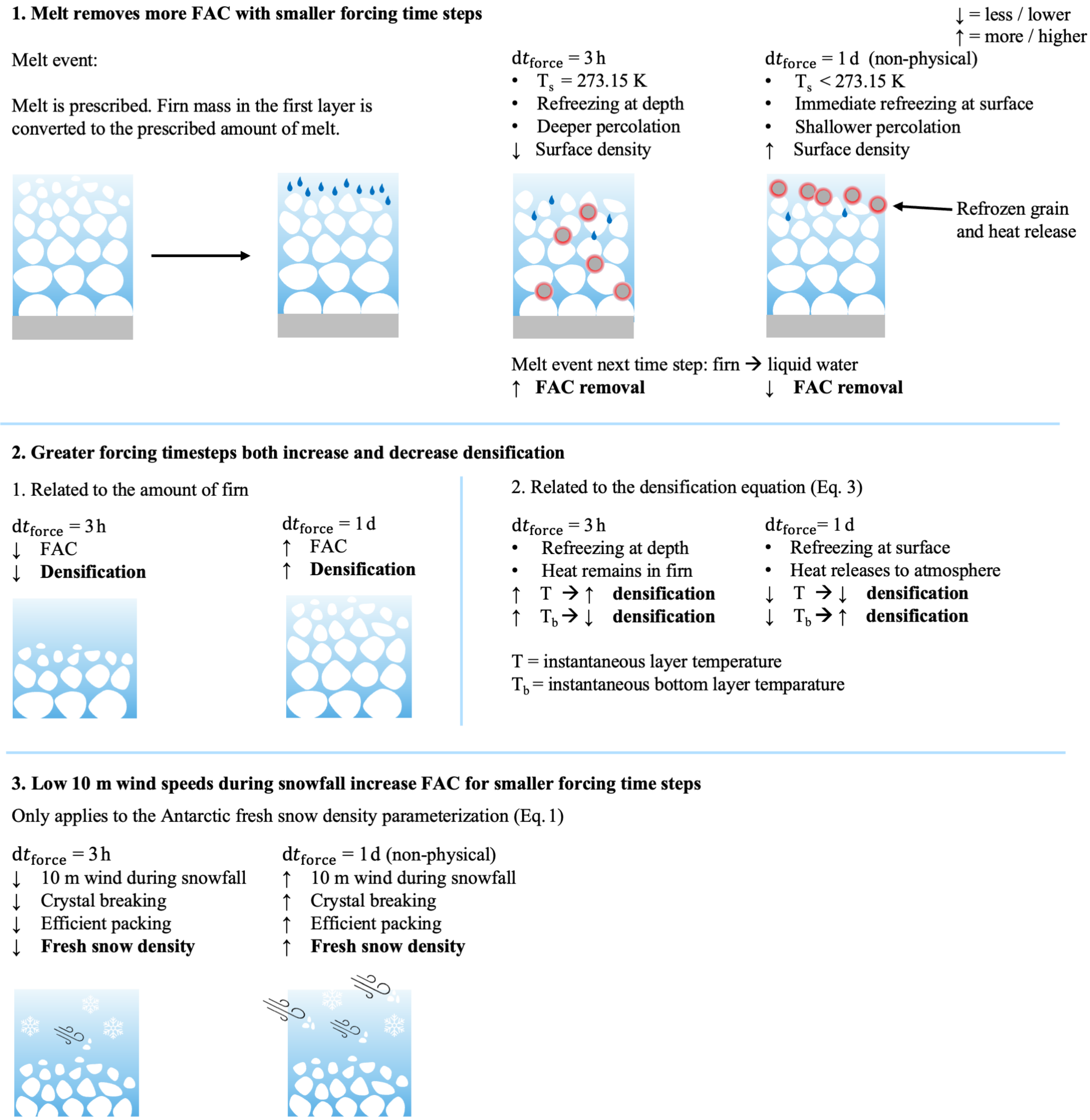

Figure 4. Processes that control (Δ)FAC. The uppermost row shows the effect of a diurnal cycle in dt_{force} on melt and refreezing, and how those influence FAC. The middle row shows that dt_{force} can both increase and decrease densification. In the lowermost row, the effect of fresh snow density parameterization in the AIS is shown.

Second, the densification rate is governed by the instantaneous layer temperature (T in Eq. 3) and the temperature of the bottom layer (T_b in Eq. 3), with higher T enhancing densification and higher T_b reducing it (Fig. 4, process 2). A similar increase in T and T_b would lead to enhanced densification (see constants in Eq. 3). Because the simulation with $dt_{force} = 3$ h has deeper refreezing (Fig. 7a compared to Fig. 7b) and warmer firn (Fig. 7c compared to Fig. 7d), the densification is indeed faster. An exception occurs when T is similar for different dt_{force} for the uppermost meters of the firn column, but T_b is higher for $dt_{force} = 3$ h due to the deeper refreezing. Then the larger approximated grain size for $dt_{force} = 3$ h slows down the densification rate, leaving more FAC.

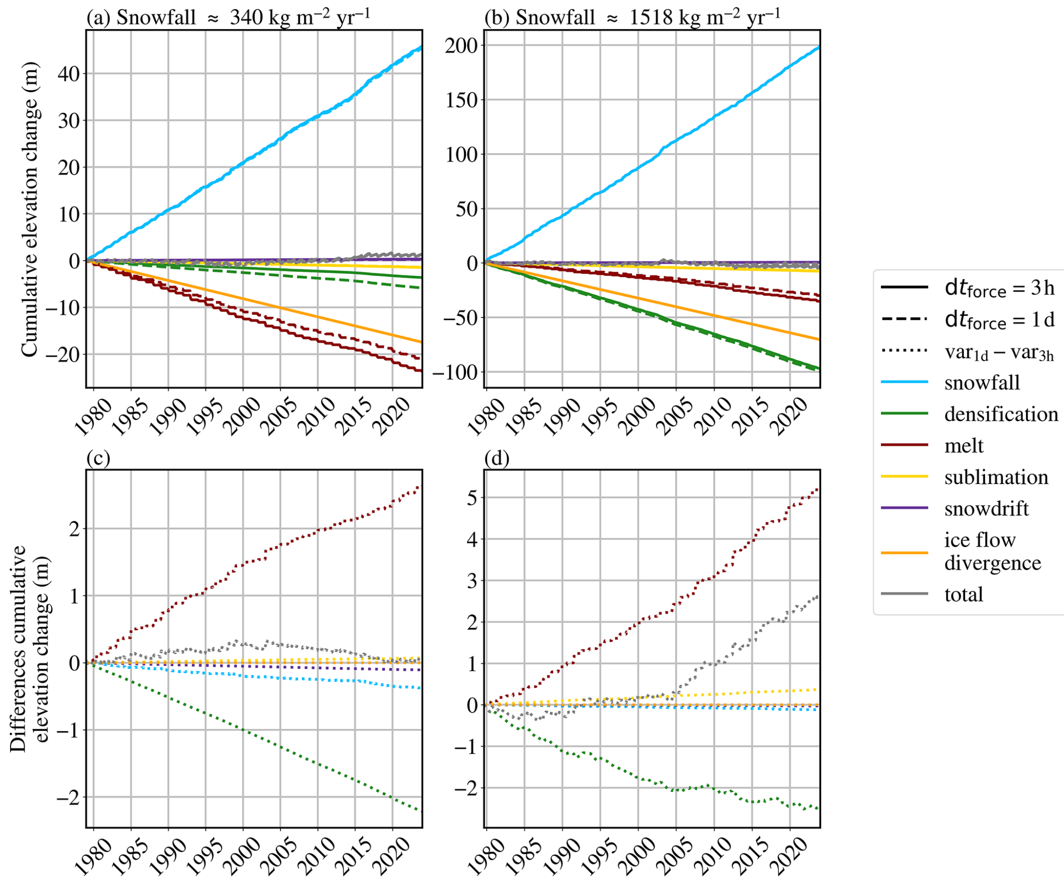

Figure 5. (a) and **(b)** Cumulative elevation change (m) due to the processes that influence the firn layer. **(c)** and **(d)** Differences in cumulative elevation change for all variables between $\mathrm{d}t_{\mathrm{force}} = 1\,\mathrm{d}$ and 3 h. Firn densification is integrated over the whole firn column. All other variables represent surface processes. Results for $\mathrm{d}t_{\mathrm{force}} = 3\,\mathrm{h}$ are in solid lines, for $\mathrm{d}t_{\mathrm{force}} = 1\,\mathrm{d}$ are in dashed lines, and the difference between the two is in dot lines. Panel **(a)** and **(c)** are a location in the APIS and panel **(b)** and **(d)** are a location in southern GrIS. Both locations experience similar melt ($\sim 340\,\mathrm{kg\,m^{-2}\,yr^{-1}}$) and $\Delta\mathrm{FAC}_{1\,\mathrm{d}}$ (2.1 m), but different snowfall. See Fig. 3a and e for a map with the grid cell locations.

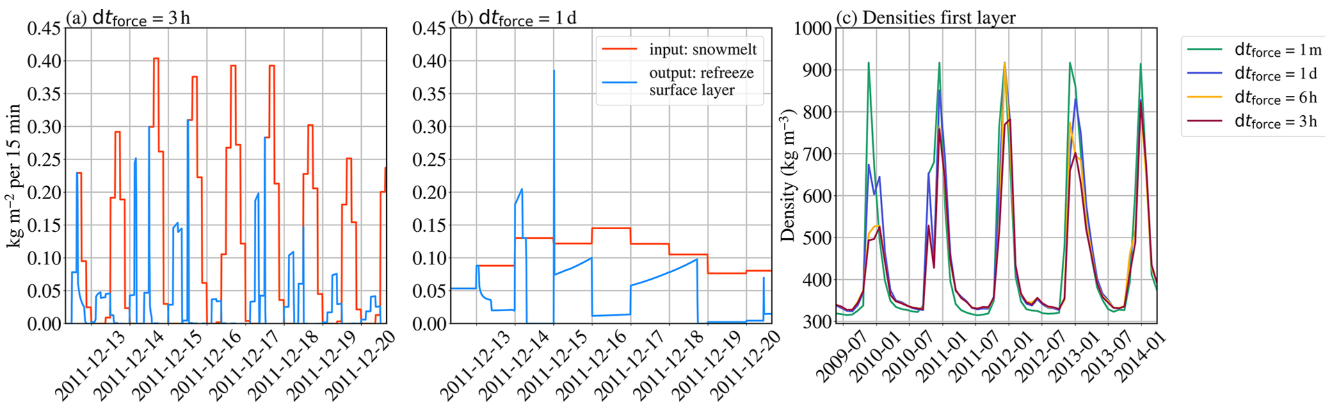

Figure 6. Snowmelt input and modelled refreezing in the surface layer for $\mathrm{d}t_{\mathrm{force}} = 3\,\mathrm{h}$ **(a)** and for $\mathrm{d}t_{\mathrm{force}} = 1\,\mathrm{d}$ **(b)**. Panel **(c)** shows the modelled densities in the surface layer. See Fig. 3a for a map with the grid cell location.

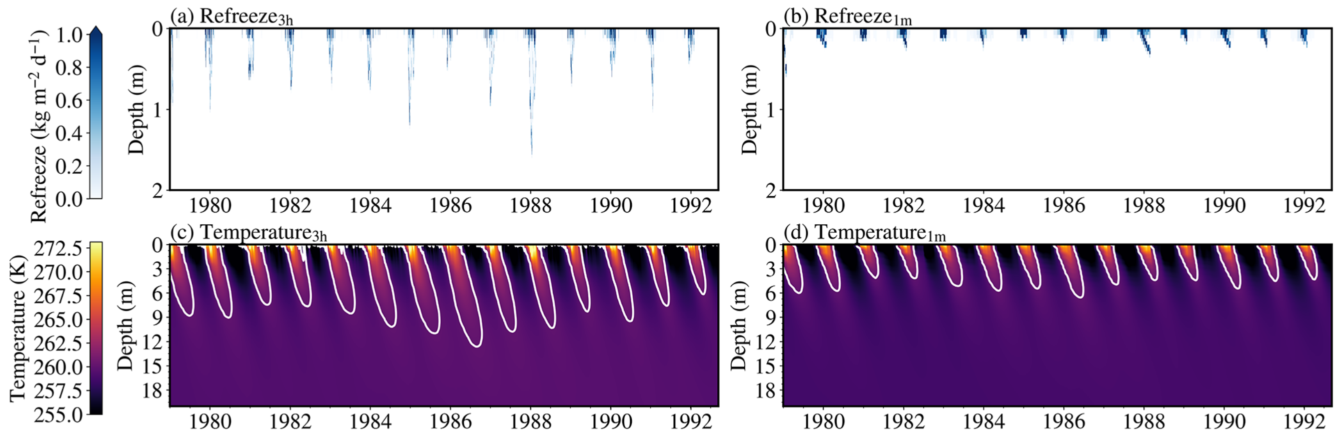

Figure 7. Refreezing amount and depth **(a, b)** and temperature profiles **(c, d)** for an example point on the APIS for $dt_{force} = 3$ h **(a, c)** and for $dt_{force} = 1$ m **(b, d)**. The white contours in panels **(c)** and **(d)** represent a temperature of 260 K. See Fig. 3a for a map with the grid cell location.

To summarize, higher firn temperatures at $dt_{force} = 3$ h increase densification rate. However, the reduction in firn depth resulting from densification (Fig. 5) remains smaller as less pore space is available to densify.

3.2.3 Process 3: fresh snow density on the APIS

An area with lower rather than higher ΔFAC is modelled in the APIS (red hues in Fig. 3b–d); this relates to differences in the estimated fresh snow density for various dt_{force}. The simulation for $dt_{force} = 3$ h has higher 10 m wind speed ($ff_{10\,m}$) variability than for larger dt_{force}, which influences fresh snow density through Eq. (1): fresh snow density increases with surface temperature T_s (Judson and Doesken, 2000) and $ff_{10\,m}$ (Sato et al., 2008). The area with negative ΔFAC typically experiences snowfall at low $ff_{10\,m}$. Lower wind speeds during snowfall lead to less crystal breaking, and therefore, less efficient packing at the surface, decreasing the fresh snow density (Fig. 4, process 3). Then, the snowfall-weighted average 10 m wind speed ($\overline{ff10\,m}^{sf}$) (Eq. 4) for $dt_{force} = 3$ h is lower than for larger dt_{force} (Fig. 8).

$$\overline{ff10\,m}^{sf} = \frac{\sum \mathrm{snowfall}(t) \times ff_{10\,m}(t)}{\sum \mathrm{snowfall}(t)} \tag{4}$$

Thus, lower $\overline{ff10\,m}^{sf}_{3\,h}$ is related to lower fresh snow densities, and therefore higher $FAC_{3\,h}$. In climate zones with limited melt ($< 30\,\mathrm{kg\,m^{-2}\,yr^{-1}}$), this effect of the fresh snow density causes a relatively small and possible negative ΔFAC of up to ±0.5 m on typical $FAC_{3\,h}$ values of 15–20 m (Fig. 3a–d).

4 Implications for IMAU-FDM

Climatic differences between the APIS and southern GrIS lead to a different response of ΔFAC to dt_{force} in IMAU-FDM. Moreover, the APIS primarily experiences a steady state climate, whereas the southern GrIS climate starts changing after 1990. The dt_{force} has different implications for steady and changing climates. Lastly, ΔFAC modifies the firn correction to altimetry. The climate and altimetry implications are discussed in the following sections for both ice sheets.

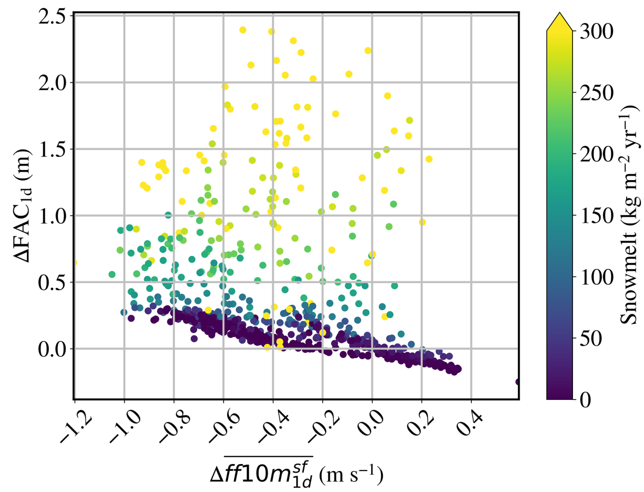

Figure 8. The $\Delta FAC_{1\,d}$ against $\Delta\overline{ff10\,m}^{sf}_{1\,d}$ in the APIS. $\Delta\overline{ff10\,m}^{sf}_{1\,d} = \overline{ff10\,m}^{sf}_{1\,d} - \overline{ff10\,m}^{sf}_{3\,h}$. In absence of melt, there is a clear relation between $\Delta\overline{ff10\,m}^{sf}_{1\,d}$ and $\Delta FAC_{1\,d}$.

4.1 APIS

Figure 9a shows that ΔFAC on the APIS increases with snowmelt. Accordingly, ice shelves have largest positive ΔFAC values (Fig. 3b–d), reflecting their relatively high snowmelt rates (Fig. 2b). Consequently, the chosen dt_{force} is crucial in assessing whether the firn air is depleted or could still buffer meltwater. Ice shelves are more vulnerable to hy-

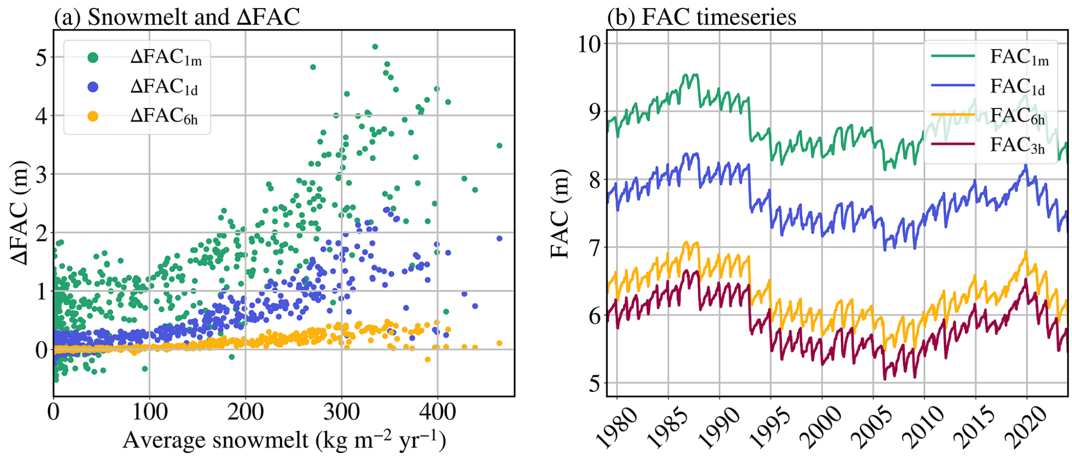

Figure 9. (a) Average $\Delta\mathrm{FAC}_{6\,\mathrm{h}}$, $\Delta\mathrm{FAC}_{1\,\mathrm{d}}$, and $\Delta\mathrm{FAC}_{1\,\mathrm{m}}$ over the simulation period against average snowmelt over 1979–2020. **(b)** FAC timeseries of one grid point on the APIS for the four $\mathrm{d}t_{\mathrm{force}}$. See Fig. 3a for a map with the grid cell location.

drofracturing when the firn air is depleted. Therefore, neglecting the daily temperature and melt cycle in firn simulations could lead to underestimated ice shelf vulnerability.

Figure 9b presents a FAC timeseries of a single grid cell on the Larsen C ice shelf (see Fig. 3 for location). The overall variations in FAC are similar across all simulations, with ΔFAC primarily established during the spin-up. The equilibrium state of the firn column has higher FAC for larger $\mathrm{d}t_{\mathrm{force}}$, where reduced FAC removal during melt events is balanced by enhanced densification.

4.2 Southern GrIS

The wider range of climatic conditions in terms of snowmelt and accumulation in the southern GrIS (Fig. 10a) compared to the APIS (Fig. 9a), complicates the isolation of processes governing ΔFAC. To facilitate the discussion, we divide the accumulation-snowmelt space into four domains (Fig. 10a).

The largest increases in $\Delta\mathrm{FAC}_{1\,\mathrm{d}}$ occur at snowmelt rates of $\sim 500\,\mathrm{kg\,m^{-2}\,yr^{-1}}$ and near a Melt-Over-Accumulation (MOA) ratio of 1 (Fig. 10a). Climate zones with snowmelt below $500\,\mathrm{kg\,m^{-2}\,yr^{-1}}$ (Fig. 10a, climate zone I), corresponding to the interior of the southern GrIS (Fig. 2e), behave similarly to the APIS: higher snowmelt rates increase $\Delta\mathrm{FAC}_{1\,\mathrm{d}}$.

Firn aquifers can form when snowmelt exceeds $500\,\mathrm{kg\,m^{-2}\,yr^{-1}}$ (Kuipers Munneke et al., 2014; Brils et al., 2024). In climate zone II (Fig. 10a and b), which are the points with annual snowmelt between 500–800 $\mathrm{kg\,m^{-2}\,yr^{-1}}$, firn aquifers formed under $\mathrm{d}t_{\mathrm{force}} = 3\,\mathrm{h}$ during spin-up, but did not for $\mathrm{d}t_{\mathrm{force}} = 1\,\mathrm{d}$. The firn has a higher heat content throughout the entire column for $\mathrm{d}t_{\mathrm{force}} = 3\,\mathrm{h}$, due to the deeper refreezing of meltwater. The higher heat content limits the refreezing capacity. We hypothesize that more liquid water remains in the firn layer and the aquifer can refill during the next melt season. In contrast, the cold content for $\mathrm{d}t_{\mathrm{force}} = 1\,\mathrm{d}$ still facilitates refreezing of all liquid water, and therefore, aquifers did not form during spin-up.

In climate zone III, snowmelt exceeds $800\,\mathrm{kg\,m^{-2}\,yr^{-1}}$ and the MOA is below 1. Firn aquifers form under both $\mathrm{d}t_{\mathrm{force}} = 3\,\mathrm{h}$ and 1 d (Fig. 10b). Here, $\Delta\mathrm{FAC}_{1\,\mathrm{d}}$ increases with snowmelt as less pore space is removed for larger $\mathrm{d}t_{\mathrm{force}}$ (Fig. 4, process 1), but this process is increasingly counterbalanced by enhanced firn densification at sites with higher accumulation (Fig. 10a). $\mathrm{FAC}_{3\,\mathrm{h}}$ is lower in this climate zone, so less pore space is available for water storage, resulting in less liquid water content (LWC) for $\mathrm{d}t_{\mathrm{force}} = 3\,\mathrm{h}$ whereas the liquid water is still retained for $\mathrm{d}t_{\mathrm{force}} = 1\,\mathrm{d}$ (Fig. 10b). More excess water for $\mathrm{d}t_{\mathrm{force}} = 3\,\mathrm{h}$ leads to more runoff. This example illustrates that the runoff limit also depends on $\mathrm{d}t_{\mathrm{force}}$ (Fig. 10c). In the southeastern GrIS, the runoff limit shifts more than 10 km inland for $\mathrm{d}t_{\mathrm{force}} = 3\,\mathrm{h}$ compared to $\mathrm{d}t_{\mathrm{force}} = 1\,\mathrm{d}$, and up to 35 km compared to $\mathrm{d}t_{\mathrm{force}} = 1\,\mathrm{m}$. This result shows that $\mathrm{d}t_{\mathrm{force}}$ plays a role in estimates of future GrIS mass balance projections.

When the MOA exceeds 1 (Fig. 10a climate zone IV), ΔFAC equals 0, as the firn is depleted in both simulations.

Unlike the example of the APIS (Fig. 9b), long-term FAC variability in Fig. 10d depends on $\mathrm{d}t_{\mathrm{force}}$ (Fig. 10d). For $\mathrm{d}t_{\mathrm{force}} = 3\,\mathrm{h}$, firn aquifers are present at the start of the simulation, whereas for $\mathrm{d}t_{\mathrm{force}} = 1\,\mathrm{d}$ they develop around 2005 (climate zone II) (Fig. 10e). In this year, the change in $\mathrm{FAC}_{1\,\mathrm{d}}$ diverges from $\mathrm{FAC}_{3\,\mathrm{h}}$, and eventually, $\mathrm{FAC}_{1\,\mathrm{d}}$ even drops below $\mathrm{FAC}_{3\,\mathrm{h}}$. This results from the densification equation (Eq. 3): liquid water in the aquifers sets the instantaneous temperature (T in Eq. 3) to 273.15 K. The bottom temperature (T_{b} in Eq. 3) is higher for $\mathrm{d}t_{\mathrm{force}} = 3\,\mathrm{h}$ (Sect. 3.2.1), because of the deeper refreezing, slowing down densification. The faster densification under $\mathrm{d}t_{\mathrm{force}} = 1\,\mathrm{d}$ reduces $\mathrm{FAC}_{1\,\mathrm{d}}$. Hence, for locations where aquifers form during the simulation, the time series of FAC (and surface elevation) become different and their trends possibly of opposite sign. This has

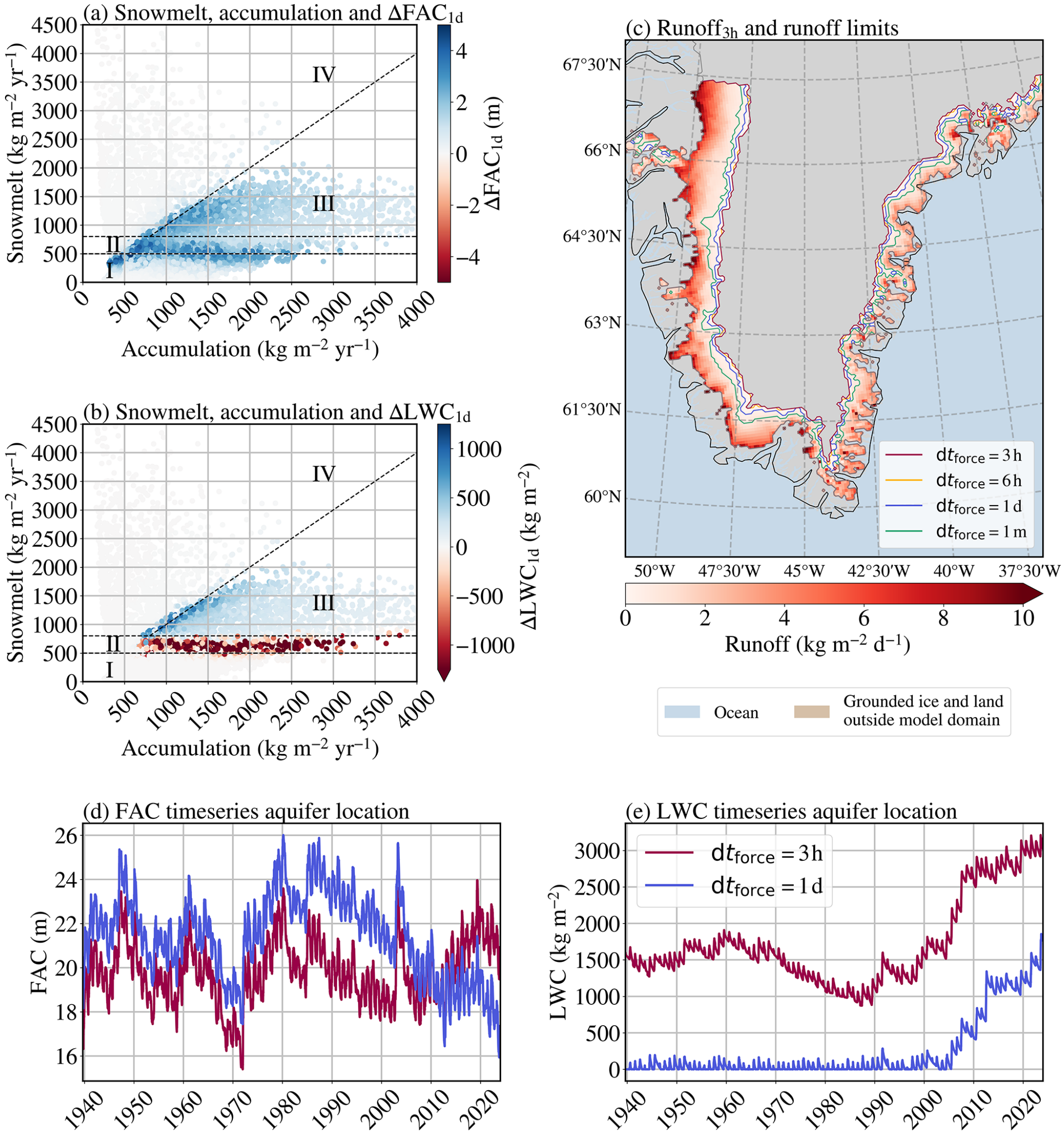

Figure 10. Average snowmelt against accumulation over 1939–1970 colour coded with average $\Delta FAC_{1\,d}$ **(a)** and $\Delta LWC_{1\,d}$ **(b)** over the simulation period. The black dashed lines represent snowmelt of 500 $kg\,m^{-2}\,yr^{-1}$ (climate zone I), 500–800 $kg\,m^{-2}\,yr^{-1}$ (climate zone II) and a MOA of 1 (separating climate zones III and IV). Panel **(c)** shows the average $runoff_{3\,h}$ over the simulation period and the different runoff limits for the four dt_{force}. Panel **(d)** and **(e)** show timeseries of respectively $FAC_{3\,h}$ and $FAC_{1\,d}$, and $LWC_{3\,h}$ and $LWC_{1\,d}$. See Fig. 3e for a map with the grid cell location.

important implications for the correct interpretation of satellite altimetry.

4.3 Implications for steady state and changing climates

Figure 9b shows an example from the APIS where the FAC differences due to dt_{force} are established during the spin-up period (1979–2020), during which the climate is assumed to be in an approximate steady state. The simulation continues for only three more years. Therefore, the ΔFAC for this location is mainly established during the spin-up period. Figure 10d shows a GrIS aquifer location, where ΔFAC develops both during and after the spin-up, which ends in 1970. The changing climate after 1970 causes $FAC_{3\,h}$ and $FAC_{1\,d}$ variations to diverge further. In this example, the ΔFAC divergence is associated with the formation of firn aquifers.

Figure A1 shows the spatial distribution of $\Delta FAC_{1\,m}$ during the last year of the simulation without the contribution from the spin-up period. The magnitude of ΔFAC established after the spin-up is larger on the GrIS than on the APIS, because the GrIS simulation covers a larger period with a changing climate. In addition, on the GrIS, the changing climate leads to formation of firn aquifers, causing the FAC to diverge after the spin-up under different dt_{force} (Fig. 10d and

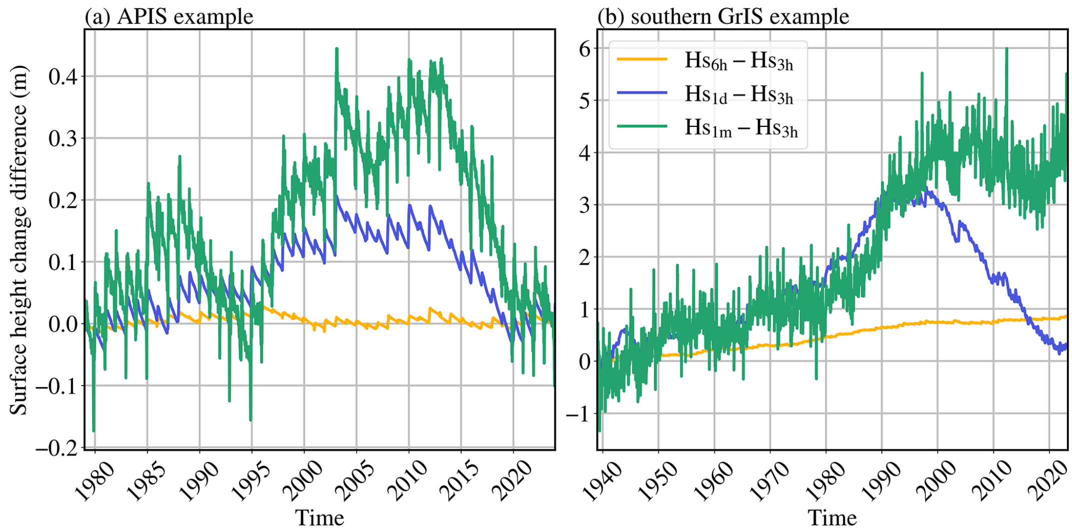

Figure 11. Differences in surface height changes over time between $dt_{force} = 3$ h and larger climate forcing time steps. Panel **(a)** represents the point in Fig. 9b and **(b)** the point in Fig. 10d and e. See Fig. 3e for a map with the grid cell location.

e). The mechanisms described in Sect. 3.2 lead to the ΔFAC differences established both during and after the spin-up.

4.4 Altimetry corrections

As simulated FAC depends on dt_{force}, then so does firn depth and hence surface height change, which is in turn used to correct altimetry data. For the same APIS sample location as shown in Fig. 9b, surface height change under $dt_{force} = 1$ d and 1 m differs from $dt_{force} = 3$ h by 0.2 and 0.4 m, respectively (Fig. 11a). ΔFAC already emerges during spin-up. At a GrIS location in transition to an aquifer, as shown in Fig. 10d and e, ΔFAC is primarily established after the spin-up and shows a stronger divergence of surface height changes, at 8 %–30 % of the FAC (Fig. 11b). Altimetry corrections based on IMAU-FDM simulations with $dt_{force} = 1$ d and 1 m would give higher surface height increases for the two examples. Consequently, during periods of ice thinning, subtracting the modeled firn depth change from the altimetry signal leads to an underestimation of ice loss, while during periods of ice thickening it leads to an underestimation of ice gain.

5 Lessons learned for firn modelling

In this section we present the lessons learned of using different dt_{force} in firn modelling. We distinguish between findings specific to IMAU-FDM and general findings.

Firn models that prescribe snowmelt fluxes and surface temperature, like IMAU-FDM, need at least a diurnal cycle in the dt_{force}. Snowmelt is the major predictor of ΔFAC, increasing ΔFAC for larger dt_{force}. Without resolving the daily cycle, snowmelt can co-exist with subfreezing surface temperatures, leading to immediate refreezing of the meltwater that is retained in the layer. This decoupling of surface temperature and snowmelt leads to non-physical results. Firn models with surface energy balance schemes that compute rather than prescribe melt fluxes might be less sensitive to this finding, but might suffer from less accurate melt fluxes.

Second, we showed how the fresh-snow density and densification parameterizations in IMAU-FDM are sensitive to dt_{force}. The fresh-snow density parameterization (Eq. 1) in the APIS is tuned specifically using $dt_{force} = 3$ h (Veldhuijsen et al., 2023). ΔFAC arising from other dt_{force} are related to the wrong use of the parameterization (Fig. 8) and are not based on physical grounds. The densification equation (Eq. 3) is based on steady state and assumes dry, non-melting snow. However, we applied the parameterization also for transient and wet conditions. The latter results in non-physical processes where the bottom temperature (T_b in Eq. 3) determines the densification rate in an aquifer and leads to different FAC variations over time for different dt_{force} (Fig. 10d and e). A general lesson learned for modelling is that the original purpose and forcing time step of a parameterization should be respected.

6 Conclusions

Ice-sheet firn models use different surface climate forcing time steps. In this study we investigated the effect of using a 3 , 6 h, 1 d, and 1-month climate forcing time step on firn air content modelled by IMAU-FDM in the Antarctic Peninsula and southern Greenland Ice Sheet.

We find that increasing the climate forcing time step typically results in more firn air (positive ΔFAC). The magnitude of this change depends on the climate regime and is most sensitive to snowmelt. More specifically, the climate forcing should resolve the diurnal cycle when surface temperature and snowmelt are prescribed at the top boundary. Otherwise, subfreezing temperatures and snowmelt can coexist, leading to immediate refreezing of the retained meltwater and, consequently, overestimating the amount of firn air.

We found that in IMAU-FDM, ΔFAC increases with snowmelt for melt rates up to $500\,\mathrm{kg\,m^{-2}\,yr^{-1}}$, across both the APIS and southern GrIS. In the latter, snowmelt rates exceeding $500\,\mathrm{kg\,m^{-2}\,yr^{-1}}$ can lead to the formation of firn aquifers. A smaller climate forcing time step results in earlier aquifer formation and therefore higher ΔFAC. Once aquifers have formed ΔFAC increases with snowmelt up to a melt-over-accumulation rate of 1, above which the firn becomes depleted for all climate forcing time steps.

In IMAU-FDM, ΔFAC was also caused by the densification and fresh snow density parameterization for non-physical reasons, i.e. when the original purpose and temporal resolution of the original parameterizations is not respected.

Ice-sheet firn air content impacts the interpretation of altimetry observations, co-determines the ice-sheet meltwater retention potential and therewith runoff limits and ice shelf vulnerability to hydrofracturing. In firn models, the climate forcing time step potentially influences the simulated firn air content and should therefore be carefully selected and tested.

Appendix A: Implications steady state and changing climate maps

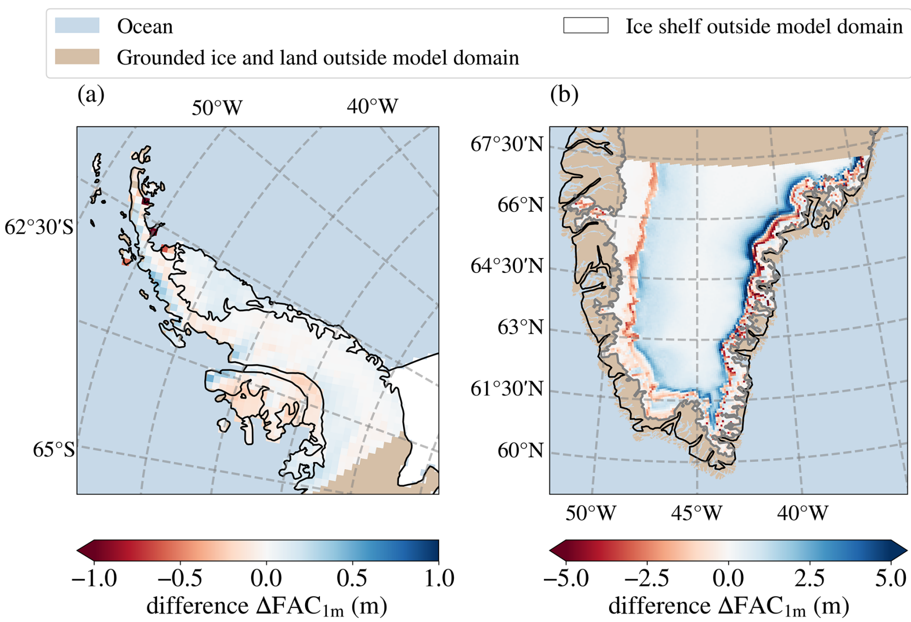

Figure A1. Differences in $\Delta FAC_{1\,m}$ between the last simulation year and the first simulation year for the APIS **(a)** and southern GrIS **(b)**. Red colours indicate that $\Delta FAC_{1\,m}$ was larger during the first simulation year, directly after the spin-up. Blue colours indicate that $\Delta FAC_{1\,m}$ was larger during the last simulation year.

Code and data availability. The IMAU-FDM v1.2A and v1.2G code is available on GitHub at https://github.com/mbrils/IMAU-FDM-v1.2 (Brils, 2021; Brils et al., 2022) or Zenodo at https://doi.org/10.5281/zenodo.5172513 (Brils et al., 2021). For this paper we updated the subroutine interpol in ini_model.f90 to interpolate the forcing data onto a 15 min model time step with a constant value, instead of the linear interpolation presented in the GitHub model version. The datasets and code to create the figures in this manuscript are available on Zenodo (https://doi.org/10.5281/zenodo.21917433, van den Aker et al., 2026). The RACMO2.3p2 forcing data is extended from the simulations of Van Wessem et al. (2018) and Noël et al. (2018). The forcing data are available upon request due to the size of the files.

Author contributions. TEAvdA, PKM, WJvdB, and MRvdB designed the study. TEAvdA performed and analyzed the simulations. All co-authors contributed to discussions on the research and manuscript.

Competing interests. At least one of the (co-)authors is a member of the editorial board of *The Cryosphere*. The peer-review process was guided by an independent editor, and the authors also have no other competing interests to declare.

Disclaimer. Publisher's note: Copernicus Publications remains neutral with regard to jurisdictional claims made in the text, published maps, institutional affiliations, or any other geographical representation in this paper. The authors bear the ultimate responsibility for providing appropriate place names. Views expressed in the text are those of the authors and do not necessarily reflect the views of the publisher.

Acknowledgements. This work was supported by EMBRACER (Summit grant no. SUMMIT.1.034), financed by the Netherlands Organization for Scientific Research (NWO). MRvdB is supported by the Horizon Europe OCEAN:ICE project (grant no. 101059388), the EMBRACER project financed by the Netherlands Organisation for Scientific Research (NWO, Summit grant SUMMIT.1.034) and the European Research Council Synergy Grant project FirnMelt (ERC grant no. 101224055). We acknowledge ECMWF for computational time on their supercomputers. We would like to thank Sanne Veldhuijsen for the origin of the idea for this project during the MSc thesis supervision, and Elizabeth Case for the improvements and development on IMAU-FDM. ChatGPT is used for figure formatting.

Financial support. This work was supported by EMBRACER (Summit grant no. SUMMIT.1.034), financed by the Netherlands Organization for Scientific Research (NWO). MRvdB is supported by the EU Horizon Europe OCEAN:ICE project (grant no. 101059388), the EMBRACER project financed by the Netherlands Organisation for Scientific Research (NWO, Summit grant SUMMIT.1.034) and the European Research Council Synergy Grant project FirnMelt (ERC grant no. 101224055).

Review statement. This paper was edited by Masashi Niwano and reviewed by two anonymous referees.

References

Arthern, R. J., Vaughan, D. G., Rankin, A. M., Mulvaney, R., and Thomas, E. R.: In situ measurements of Antarctic snow compaction compared with predictions of models, J. Geophys. Res.-Earth, 115, https://doi.org/10.1029/2009JF001306, 2010.

Brils, M.: IMAU-FDM-v1.2, GitHub [code], https://github.com/mbrils/IMAU-FDM-v1.2, last access: 9 August 2021.

Brils, M., Kuipers Munneke, P., Van de Berg, W. J., and Van den Broeke, M.: IMAU-FDM v1 GDM release, Zenodo [code], https://doi.org/10.5281/zenodo.5172513, 2021.

Brils, M., Kuipers Munneke, P., van de Berg, W. J., and van den Broeke, M.: Improved representation of the contemporary Greenland ice sheet firn layer by IMAU-FDM v1.2G, Geosci. Model Dev., 15, 7121–7138, https://doi.org/10.5194/gmd-15-7121-2022, 2022.

Brils, M., Munneke, P. K., Jullien, N., Tedstone, A., Machguth, H., Van De Berg, W., and Van Den Broeke, M.: Climatic drivers of ice slabs and firn aquifers in Greenland, Geophys. Res. Lett., 51, e2023GL106613, https://doi.org/10.1029/2023GL106613, 2024.

Calonne, N., Milliancourt, L., Burr, A., Philip, A., Martin, C. L., Flin, F., and Geindreau, C.: Thermal conductivity of snow, firn, and porous ice from 3-D image-based computations, Geophys. Res. Lett., 46, 13079–13089, https://doi.org/10.1029/2019GL085228, 2019.

Coléou, C. and Lesaffre, B.: Irreducible water saturation in snow: experimental results in a cold laboratory, Ann. Glaciol., 26, 64–68, https://doi.org/10.3189/1998AoG26-1-64-68, 1998.

Fausto, R. S., Box, J. E., Vandecrux, B., Van As, D., Steffen, K., MacFerrin, M. J., Machguth, H., Colgan, W., Koenig, L. S., McGrath, D., Charalampidis, C., and Braithwaite, R. J.: A snow density dataset for improving surface boundary conditions in Greenland ice sheet firn modeling, Front. Earth Sci., 6, 51, https://doi.org/10.3389/feart.2018.00051, 2018.

Gkinis, V., Holme, C., Kahle, E. C., Stevens, M. C., Steig, E. J., and Vinther, B. M.: Numerical experiments on firn isotope diffusion with the Community Firn Model, J. Glaciol., 67, 450–472, https://doi.org/10.1017/jog.2021.1, 2021.

Hansen, N., Orr, A., Zou, X., Boberg, F., Bracegirdle, T. J., Gilbert, E., Langen, P. L., Lazzara, M. A., Mottram, R., Phillips, T., Price, R., Simonsen, S. B., and Webster, S.: The importance of cloud properties when assessing surface melting in an offline-coupled firn model over Ross Ice shelf, West Antarctica, The Cryosphere, 18, 2897–2916, https://doi.org/10.5194/tc-18-2897-2024, 2024.

Helsen, M. M., Van Den Broeke, M. R., Van De Wal, R. S., Van De Berg, W. J., Van Meijgaard, E., Davis, C. H., Li, Y., and Goodwin, I.: Elevation changes in Antarctica mainly determined by accumulation variability, Science, 320, 1626–1629, https://doi.org/10.1126/science.1153894, 2008.

Hersbach, H., Bell, B., Berrisford, P., Hirahara, S., Horányi, A., Muñoz-Sabater, J., Nicolas, J., Peubey, C., Radu, R., Schepers, D., Simmons, A., Soci, C., Abdalla, S., Abellan, X., Balsamo, G., Bechtold, P., Biavati, G., Bidlot, J., Bonavita, M., De Chiara, G., Dahlgren, P., Dee, D., Diamantakis, M., Dragani, R., Flemming, J., Forbes, R., Fuentes, M., Geer, A., Haimberger, L., Healy, S., Hogan, R. J., Hólm, E., Janisková, M., Keeley, S., Laloyaux, P., Lopez, P., Lupu, C., Radnoti, G., de Rosnay, P., Rozum, I., Vamborg, F., Villaume, S., and Thépaut, J.-N.: The ERA5 global reanalysis, Q. J. Roy. Meteor. Soc., 146, 1999–2049, https://doi.org/10.1002/qj.3803, 2020.

Judson, A. and Doesken, N.: Density of freshly fallen snow in the central Rocky Mountains, B. Am. Meteorol. Soc., 81, 1577–1588, https://doi.org/10.1175/1520-0477(2000)081<1577:DOFFSI>2.3.CO;2, 2000.

Kuipers Munneke, P., M. Ligtenberg, S., Van Den Broeke, M., Van Angelen, J., and Forster, R.: Explaining the presence of perennial liquid water bodies in the firn of the Greenland Ice Sheet, Geophys. Res. Lett., 41, 476–483, https://doi.org/10.1002/2013GL058389, 2014.

Kuipers Munneke, P., Ligtenberg, S. R. M., Noël, B. P. Y., Howat, I. M., Box, J. E., Mosley-Thompson, E., McConnell, J. R., Steffen, K., Harper, J. T., Das, S. B., and van den Broeke, M. R.: Elevation change of the Greenland Ice Sheet due to surface mass balance and firn processes, 1960–2014, The Cryosphere, 9, 2009–2025, https://doi.org/10.5194/tc-9-2009-2015, 2015.

Langen, P. L., Fausto, R. S., Vandecrux, B., Mottram, R. H., and Box, J. E.: Liquid water flow and retention on the Greenland ice sheet in the regional climate model HIRHAM5: local and large-scale impacts, Front. Earth Sci., 4, 110, https://doi.org/10.3389/feart.2016.00110, 2017.

Lenaerts, J. T., Van den Broeke, M., Déry, S., Van Meijgaard, E., Van de Berg, W., Palm, S. P., and Sanz Rodrigo, J.: Modeling drifting snow in Antarctica with a regional climate model: 1. Methods and model evaluation, J. Geophys. Res.-Atmos., 117, https://doi.org/10.1029/2011JD016145, 2012.

Ligtenberg, S. R. M., Helsen, M. M., and van den Broeke, M. R.: An improved semi-empirical model for the densification of Antarctic firn, The Cryosphere, 5, 809–819, https://doi.org/10.5194/tc-5-809-2011, 2011.

Ligtenberg, S. R. M., Kuipers Munneke, P., and van den Broeke, M. R.: Present and future variations in Antarctic firn air content, The Cryosphere, 8, 1711–1723, https://doi.org/10.5194/tc-8-1711-2014, 2014.

Medley, B., Neumann, T. A., Zwally, H. J., Smith, B. E., and Stevens, C. M.: Simulations of firn processes over the Greenland and Antarctic ice sheets: 1980–2021, The Cryosphere, 16, 3971–4011, https://doi.org/10.5194/tc-16-3971-2022, 2022.

Meyer, C. R. and Hewitt, I. J.: A continuum model for meltwater flow through compacting snow, The Cryosphere, 11, 2799–2813, https://doi.org/10.5194/tc-11-2799-2017, 2017.

Noël, B., van de Berg, W. J., van Wessem, J. M., van Meijgaard, E., van As, D., Lenaerts, J. T. M., Lhermitte, S., Kuipers Munneke, P., Smeets, C. J. P. P., van Ulft, L. H., van de Wal, R. S. W., and van den Broeke, M. R.: Modelling the climate and surface mass balance of polar ice sheets using RACMO2 – Part 1: Greenland (1958–2016), The Cryosphere, 12, 811–831, https://doi.org/10.5194/tc-12-811-2018, 2018.

Noël, B., Lenaerts, J. T., Lipscomb, W. H., Thayer-Calder, K., and van den Broeke, M. R.: Peak refreezing in the Greenland firn layer under future warming scenarios, Nat. Commun., 13, 6870, https://doi.org/10.1038/s41467-022-34524-x, 2022.

Sato, T., Kosugi, K., Mochizuki, S., and Nemoto, M.: Wind speed dependences of fracture and accumulation of snowflakes on snow surface, Cold Reg. Sci. Technol., 51, 229–239, https://doi.org/10.1016/j.coldregions.2007.05.004, 2008.

Shepherd, A., Ivins, E. R., A, G., Barletta, V. R., Bentley, M. J., Bettadpur, S., Briggs, K. H., Bromwich, D. H., Forsberg, R., Galin, N., Horwath, M., Jacobs, S., Joughin, I., King, M. A., Lenaerts, J. T. M., Li, J., Ligtenberg, S. R. M., Luckman, A., Luthcke, S. B., McMillan, M., Meister, R., Milne, G., Mouginot, J., Muir, A., Nicolas, J. P., Paden, J., Payne, A. J., Pritchard, H., Rignot, E., Rott, H., Sandberg Sørensen, L., Scambos, T. A., Scheuchl, B., Schrama, E. J. O., Smith, B., Sundal, A. V., van Angelen, J. H., van de Berg, W. J., van den Broeke, M. R., Vaughan, D. G., Velicogna, I., Wahr, J., Whitehouse, P. L., Wingham, D. J., Yi, D., Young, D., and Zwally, H. J.: A reconciled estimate of ice-sheet mass balance, Science, 338, 1183–1189, https://doi.org/10.1126/science.1228102, 2012.

Simonsen, S. B., Stenseng, L., Adalgeirsdottir, G., Fausto, R. S., Hvidberg, C. S., and Lucas-Picher, P.: Assessing a multilayered dynamic firn-compaction model for Greenland with ASIRAS radar measurements, J. Glaciol., 59, 545–558, https://doi.org/10.3189/2013JoG12J158, 2013.

Sørensen, L. S., Simonsen, S. B., Nielsen, K., Lucas-Picher, P., Spada, G., Adalgeirsdottir, G., Forsberg, R., and Hvidberg, C. S.: Mass balance of the Greenland ice sheet (2003–2008) from ICESat data – the impact of interpolation, sampling and firn density, The Cryosphere, 5, 173–186, https://doi.org/10.5194/tc-5-173-2011, 2011.

Stevens, C. M., Verjans, V., Lundin, J. M. D., Kahle, E. C., Horlings, A. N., Horlings, B. I., and Waddington, E. D.: The Community Firn Model (CFM) v1.0, Geosci. Model Dev., 13, 4355–4377, https://doi.org/10.5194/gmd-13-4355-2020, 2020.

The Firn Symposium Team: Firn on ice sheets, Nature Reviews Earth and Environment, 5, 79–99, https://doi.org/10.1038/s43017-023-00507-9, 2024.

Thompson-Munson, M., Wever, N., Stevens, C. M., Lenaerts, J. T. M., and Medley, B.: An evaluation of a physics-based firn model and a semi-empirical firn model across the Greenland Ice Sheet (1980–2020), The Cryosphere, 17, 2185–2209, https://doi.org/10.5194/tc-17-2185-2023, 2023.

Vandecrux, B., Mottram, R., Langen, P. L., Fausto, R. S., Olesen, M., Stevens, C. M., Verjans, V., Leeson, A., Ligtenberg, S., Kuipers Munneke, P., Marchenko, S., van Pelt, W., Meyer, C. R., Simonsen, S. B., Heilig, A., Samimi, S., Marshall, S., Machguth, H., MacFerrin, M., Niwano, M., Miller, O., Voss, C. I., and Box, J. E.: The firn meltwater Retention Model Intercomparison Project (RetMIP): evaluation of nine firn models at four weather station sites on the Greenland ice sheet, The Cryosphere, 14, 3785–3810, https://doi.org/10.5194/tc-14-3785-2020, 2020.

van den Aker, T. E. A., Kuipers Munneke, P., van de Berg, W. J., Immerzeel, W., and van den Broeke, M. R.: Datasets and plotting code: Impact of climate forcing time step in an ice-sheet firn model, Zenodo [data set], https://doi.org/10.5281/zenodo.21917433, 2026.

van Wessem, J. M., van de Berg, W. J., Noël, B. P. Y., van Meijgaard, E., Amory, C., Birnbaum, G., Jakobs, C. L., Krüger, K., Lenaerts, J. T. M., Lhermitte, S., Ligtenberg, S. R. M., Medley, B., Reijmer,

C. H., van Tricht, K., Trusel, L. D., van Ulft, L. H., Wouters, B., Wuite, J., and van den Broeke, M. R.: Modelling the climate and surface mass balance of polar ice sheets using RACMO2 – Part 2: Antarctica (1979–2016), The Cryosphere, 12, 1479–1498, https://doi.org/10.5194/tc-12-1479-2018, 2018.

Veldhuijsen, S. B. M., van de Berg, W. J., Brils, M., Kuipers Munneke, P., and van den Broeke, M. R.: Characteristics of the 1979–2020 Antarctic firn layer simulated with IMAU-FDM v1.2A, The Cryosphere, 17, 1675–1696, https://doi.org/10.5194/tc-17-1675-2023, 2023.

Verjans, V., Leeson, A. A., Stevens, C. M., MacFerrin, M., Noël, B., and van den Broeke, M. R.: Development of physically based liquid water schemes for Greenland firn-densification models, The Cryosphere, 13, 1819–1842, https://doi.org/10.5194/tc-13-1819-2019, 2019.

Wang, W., Shen, Y., Chen, Q., and Wang, F.: Unprecedented mass gain over the Antarctic ice sheet between 2021 and 2022 caused by large precipitation anomalies, Environ. Res. Lett., 18, 124012, https://doi.org/10.1088/1748-9326/ad0863, 2023.

Wever, N., Keenan, E., Amory, C., Lehning, M., Sigmund, A., Huwald, H., and Lenaerts, J. T.: Observations and simulations of new snow density in the drifting snow-dominated environment of Antarctica, J. Glaciol., 69, 823–840, https://doi.org/10.1017/jog.2022.102, 2023.

Winther, J.-G., Jespersen, M. N., and Liston, G. E.: Blue-ice areas in Antarctica derived from NOAA AVHRR satellite data, J. Glaciol., 47, 325–334, https://doi.org/10.3189/172756501781832386, 2001.

Zhang, X., Liu, L., Noël, B., and Luo, Z.: Modelling firn density at Dye-2 and KAN_U, two sites in the percolation zone of the Greenland ice sheet, EGUsphere [preprint], https://doi.org/10.5194/egusphere-2024-1726, 2024.